THE ASTROPHYSICAL JOURNAL, 355:182–189, 1990 May 20

SPECTROSCOPY OF EXTENDED RED EMISSION IN REFLECTION NEBULAE

ADOLF N. WITT
Ritter Astrophysical Research Center
AND
TODD A. BOROSON
Kitt Peak National Observatory, National Optical Astronomy Observatories
Received 1989 October 23; accepted 1989 November 28

ABSTRACT

We report the results of a spectroscopic survey of reflection nebulae, aimed at studying the characteristics of the broad emission feature responsible for the extended red emission (ERE) observed in these objects. The ERE band was detected and its strength, central wavelength, and width were measured in 12 nebulae, while upper limits were recorded in 12 further objects. The maximum ERE band intensity was found to vary from object to object within an extremely narrow range while the associated scattered light intensities differed by nearly two orders of magnitude. We interpret the ERE band as arising from the photoluminescence of hydrogenated amorphous carbon (HAC) grains which become rehydrogenated and gain luminescence efficiency in narrow H_2 photodissociation zones. These zones are probably thin shells around the exciting stars. Observed changes in the central wavelengths and widths of the ERE bands detected in different parts of a given nebula, and from nebula to nebula, support the HAC model and are explained as arising from variations in the degree of hydrogenation of the solid grains. The Red Rectangle, while emitting the ERE band with unusual strength, is found to be an object of a class different from ordinary reflection nebulae. The luminescent material pervades the entire nebula and appears to be produced in a local mass-loss process rather than through rehydrogenation.

Subject headings: nebulae: reflection — radiation mechanisms

I. INTRODUCTION

Witt and Schild (1988, hereafter WS) showed the extended red emission (ERE) observed in numerous reflection nebulae (Witt, Schild, and Kraiman 1984; Witt and Schild 1985, 1986) to be at least in part due to a broad luminescence band, centered between λ6500 and λ7000 wavelength, which they attributed to photoluminescence by hydrogenated amorphous carbon grains. The full extent in wavelength of the ERE band was not revealed by the WS data, due to insufficient spectral coverage resulting in part from the limits in spectral sensitivity of the detector. Thus, WS were unable to derive absolute band intensities. Also, their spatial resolution (beam size 45″) was insufficient to fully delineate the spatial variation of the band intensity and profile across individual nebulae, but they did provide the initial evidence suggesting that such changes might be present. In the current work, at some expense of spectral resolution, we have increased the spectral range and spatial resolution to allow us to address these aspects now in more detail. We also have extended our spectroscopic observations to a considerably larger number of reflection nebulae, which have been studied previously by photometric methods only.

II. OBSERVATIONS AND REDUCTION

Spectroscopic observations of a number of reflection nebulae were obtained on two observing runs with the McGraw-Hill Observatory 1.3 m telescope and the Mark III spectrograph. This spectrograph, which uses all transmitting optics, has the advantages of high throughput and a large usable field. In the first run, 1986 December 9–13, the detector used was a thick GEC CCD. In the second run, 1987 December 4–8, a thick Thompson CCD was used. These two CCDs have quite similar formats (385 × 576 pixels, with 22 μm pixels) and properties. For both runs, a 150 lines mm^{-1} grism blazed at λ8850 and a 7″.8 wide slit were used. Because of the wide slit and the fact that the surface brightness of the nebulae is low, the pixels were binned as they were read out such that 4 pixels in the spatial direction and 2 in the spectral direction were combined. The resulting images have scales of approximately 21.6 Å $pixel^{-1}$ from λ5000 to λ9000, and 5″.25 $pixel^{-1}$ over about 7′ of slit length. The slit projected to about 3 pixels, limiting the spectral resolution to approximately 60 Å.

Observations of Galactic reflection nebulae in order to study the ERE are complicated by two facts. First, the nebulae are quite extended, so that sky subtraction is difficult, particularly in the red where the sky emission is bright and variable. Second, a large (and unknown) fraction of the light from the nebulae is the scattered spectrum of the illuminating star. Since this contribution must be accurately subtracted in order to detect and measure the ERE, we adopted an observing procedure designed to simplify this process. The nebular observations were limited to 1800 s exposures with each integration being sandwiched between two short exposures of the illuminating star. If the region of interest was faint, multiple exposures were made. We positioned the slit either north-south or east-west in order to observe the nebular regions of interest and to ensure that some part of the slit would sample the sky. Because of the wide slit and the fact that the scattering is a function of wavelength, we did not worry about the effect of atmospheric refraction but assumed that the wavelength dependence of scattering would have to be determined in the reduction stage.

A number of nebulae were observed, and multiple slit positions were used in some cases, especially where WS had found evidence for strong variations in the ERE intensity. A journal of the observation is given in Table 1. This table gives a chro-

TABLE 1

JOURNAL OF OBSERVATIONS

Sequence Number	Object	Date	Exposure (s)	Slit PA	Slit Position
1.....	NGC 1333	1986 Dec 9	2 × 1800	NS	Slit just S of BD +30°549
2.....	Red Rectangle	1989 Dec 9	900	NS	Slit 6″ E of HD 44179
3.....	NGC 2327	1986 Dec 9	2 × 1800	NS	Slit 8″ W of star
4.....	NGC 2071	1986 Dec 9	1800	NS	Slit just S of HD 290861
5.....	DG 87	1986 Dec 9	1800	NS	Slit 7″ W of star
6.....	Merope	1986 Dec 10	1800	EW	HD 23480 35″ N of W end of slit
7.....	NGC 2247	1986 Dec 10	1800	EW	Slit 12″ S of HD 259431
8.....	Merope	1986 Dec 11	2 × 1800	EW	HD 23480 35″ N of W end of slit
9.....	Merope	1986 Dec 11	1800	EW	Slit 12′ S of HD 23480
10.....	IC 348	1986 Dec 11	1800	EW	Slit 15″ S of HD 281159
11.....	IC 435	1986 Dec 11	2 × 1800	EW	Slit 10″ S of HD 38087
12.....	NGC 1333	1986 Dec 12	2 × 1800	EW	Slit 10″ S of BD +30°549
13.....	Maja	1986 Dec 12	1800	EW	HD 23408 30″ N of E end of slit
14.....	NGC 1788	1986 Dec 12	2 × 1800	EW	Slit 5″ N of HD 293815
15.....	IC 426	1986 Dec 12	1800	EW	HD 37140 10″ N of W end of slit
16.....	NGC 2068	1986 Dec 12	2 × 1800	EW	Slit 15″ S of HD 38563N
17.....	NGC 2068	1986 Dec 12	1800	EW	Slit 15″ N of HD 38563N
18.....	NGC 1999	1986 Dec 12	1800	EW	Slit 10″ N of V 380 ORI
19.....	NGC 2023	1986 Dec 12	1800	EW	Slit 40″ N of HD 37903
20.....	IC 59	1987 Dec 4	1800	NS	Slit just N of γ Cas
21.....	IC 63	1987 Dec 4	1800	NS	Slit E of γ Cas
22.....	NGC 7023	1987 Dec 5	1800	NS	HD 200775 just E of S end of slit
23.....	NGC 7023	1987 Dec 6	1800	NS	HD 200775 20″ W of HD 200775
24.....	NGC 7129	1987 Dec 6	1800	NS	Slit between BD +65°1637 and BD +65°1638
25.....	Ced 201	1987 Dec 6	1800	NS	Slit 10″ E of BD +69°1231
26.....	Red Rectangle	1987 Dec 6	2 × 600	EW	Slit 10″ S of HD 44179
27.....	Red Rectangle	1987 Dec 6	2 × 600	EW	Slit 6″ S of HD 44179
28.....	Red Rectangle	1987 Dec 6	2 × 600	EW	Slit 7″ N of HD 44179
29.....	Red Rectangle	1987 Dec 6	1800	EW	Slit 14″ N of HD 44179
30.....	Ced 167	1987 Dec 7	1800	EW	Slit 6″ S of HD 182918
31.....	vdB 132	1987 Dec 7	1800	EW	Slit 20″ N of BD +41°3737
32.....	IC 5076	1987 Dec 7	1800	EW	Slit 60″ S of HD 199478
33.....	NGC 2023	1987 Dec 7	1800	EW	Slit 15″ N of HD 37903
34.....	NGC 2023	1987 Dec 7	1800	EW	Slit 30″ N of HD 37903

nological listing of the nebulae observed with separate entries for each different slit position used. Throughout the two observing runs, dome flat fields and bias frames were obtained, and during each night, spectrophotometric standard stars and comparison lamps were observed several times.

The raw frames were corrected in the usual way for bias and flat-field variations and were carefully rectified geometrically such that the slit and the dispersion were as straight and parallel to the CCD rows and columns as possible. The sky was subtracted two-dimensionally from each frame by choosing one or more regions along the slit which were relatively free from nebular light. If only one such region was available, an average value was determined for each wavelength and subtracted from each pixel in that column (perpendicular to the dispersion) of the frame. If two or more sky regions could be used, a linear fit was made to the intensity in a column, and this was used to calculate an interpolated sky value for each pixel in that column.

The extraction of one-dimensional spectra was carried out by choosing the regions of interest along the slit for each object. Usually this was done by noting where the nebular light was most intense. In some cases, the slit length was divided into several regions. The one-dimensional spectra were then constructed by summing the counts along each column from the rows which corresponded to that region or regions. The spectra of the comparison lamp and the spectrophotometric standard stars were extracted in the same way.

These spectra were then wavelength calibrated, rebinned to a common wavelength scale, corrected for atmospheric extinction, and flux-calibrated. The spectra of the illuminating stars which were obtained before and after each nebular observation were combined, as were the nebular spectra in those cases where multiple observations were made.

The next step in the reduction procedure was to attempt to separate the starlight scattered in the nebula from the emission intrinsic to the nebula. The assumption was made that the scattered light was well respresented by a continuum of the form $r \cdot F(\lambda) \cdot \lambda^{-p}$, where r is a scaling constant, $F(\lambda)$ is the spectrum of the illuminating star and p is a power which depends on the details of the scatterers. For each object, r and p were determined from the intercept and slope of a line fit to the nebular spectrum divided by the star spectrum. This fit was made in two regions which bracket the position of the ERE, $\lambda\lambda$5000–5500 and $\lambda\lambda$8500–9000. Then, using these derived parameters, the scattered light was subtracted from the total nebular spectrum for each object.

In order to characterize the ERE, several quantities were measured from each of the spectra. First, the total flux between λ5500 and λ8500 was measured from each of the corrected and uncorrected spectra. When obvious emission lines were present, these were measured also and their flux subtracted from the band measurements. Using the known value for the area of sky observed in each case, these fluxes were converted to units of ergs cm^2 s^{-1} sr^{-1}. The ratio of ERE flux to scat-

TABLE 2

EXTENDED RED EMISSION DETECTIONS

Sequence Number	Object	p	I(ERE) (ergs cm^{-2} s^{-1} sr^{-1})	λ_c (Å)	$\Delta\lambda$ (Å)	ERE/Scat	W (arcsec^2)
1.....	NGC 1333	0.6	3.6 (−5)	...	...	0.07	1146
2.....	Red Rectangle	0.0	2.6 (−3)	6643	770	0.53	369
3.....	NGC 2327	0.5	1.1 (−4)	7011	915	0.06	696
5.....	DG 87	1.2	6.0 (−5)	...	...	0.04	696
7.....	NGC 2247	0.9	2.5 (−4)	6852	750	0.08	696
12.....	NGC 1333	1.2	1.4 (−4)	6770	810	0.16	655
15.....	IC 426	−2.8	5.1 (−5)	6587	680	0.21	614
18.....	NGC 1999	2.0	2.7 (−4)	...	...	0.06	696
21.....	IC 63	−1.8	9.8 (−5)	...	...	0.68	450
22.....	NGC 7023	0.5	1.3 (−4)	6884	980	0.12	573
	NGC 7023	−0.8	1.1 (−4)	6946	840	0.14	287
23.....	NGC 7023	0.6	1.6 (−4)	6862	820	0.04	901
	NGC 7023	0.1	2.1 (−4)	6871	760	0.15	328
	NGC 7023	1.2	4.0 (−5)	6568	620	0.04	164
	NGC 7023	0.4	1.3 (−4)	6902	780	0.12	328
24.....	NGC 7129	0.5	2.1 (−5)	6626	800	0.08	1996
25.....	Ced 201	0.4	3.1 (−5)	7009	720	0.02	778
26.....	Red Rectangle	0.4	2.0 (−3)	6590	760	1.00	369
27.....	Red Rectangle	−0.2	7.1 (−3)	6839	920	1.06	328
28.....	Red Rectangle	0.5	3.0 (−3)	6581	740	1.25	328
29.....	Red Rectangle	0.7	4.0 (−3)	6522	700	0.70	450
33.....	NGC 2023	0.3	1.2 (−4)	6673	620	0.29	82
34.....	NGC 2023	0.0	1.4 (−4)	6822	800	0.42	82

tered flux was then determined from these numbers. The corrected spectra are in some cases fairly noisy, and so it was decided to attempt to characterize them with just two numbers representing a central position and a width. The center of the band was determined by a luminosity-weighted centroid, i.e., the wavelength which splits the band luminosity into two equal parts. A similar scheme was adopted for the width. It was measured as the difference between the wavelengths of the first and third quartiles. These quantities should be relatively immune to noise as they depend on the integrated emission more than on the details of the shape or highest point in the band.

Tables 2 and 3 present these measurements for all the objects which were observed. In Table 2 the detections of the ERE are shown. For each object, the following quantities are given: the slope of the scattering function (p in the formula above), the integrated flux in the ERE band, the central wavelength of the band, the width of the band, the ratio of the band flux to the scattered flux, and the area measured in square arcseconds. In a few cases, the signal-to-noise ratio was considered too low to even roughly determine central wavelength and width. Table 3 shows the observations for which only an upper limit on ERE strength could be determined. This table gives the total flux measured in the nebula, a 1 σ estimate of the upper limit on the ERE to scattered light ratio, and the area measured.

III. RESULTS

a) *The ERE Band Intensities*

We plotted the measured ERE band intensities I_{ERE} (Table 2) and the upper limits (Table 3) as a function of the integrated ($\lambda\lambda$5500–8500) scattered light intensity I_{SCA} in Figure 1. Shown as diagonal lines are loci of constant ratios of I_{ERE}/I_{SCA} in percent.

TABLE 3

EXTENDED RED EMISSION UPPER LIMITS

Sequence Number	Object	P	I(Tot) (ergs cm^{-2} s^{-1} sr^{-1})	ERE/Scat	W (arcsec^2)
4.....	NGC 2071	...	1.7 (−3)	<0.090	860
6.....	Merope	1.74	8.0 (−3)	<0.006	942
8.....	Merope	...	5.0 (−3)	<0.007	1188
9.....	Merope	−0.5	2.9 (−4)	<0.053	942
10.....	IC 348	1.74	1.6 (−3)	<0.046	1228
11.....	IC 435	1.12	1.7 (−3)	<0.010	942
13.....	Maja	1.25	4.4 (−3)	<0.016	1720
14.....	NGC 1788	0.20	1.1 (−3)	<0.026	1065
16.....	NGC 2068	3.67	3.4 (−3)	<0.025	1147
17.....	NGC 2068	2.68	2.3 (−3)	<0.028	1188
19.....	NGC 2023	0.60	1.4 (−3)	<0.015	1679
20.....	IC 59	−2.00	1.5 (−4)	<0.160	1679
30.....	Ced 167	−0.35	2.0 (−3)	<0.013	778
31.....	vdB 132	−0.20	1.2 (−4)	<0.020	1228
32.....	IC 5076	−0.00	1.4 (−4)	<0.093	901

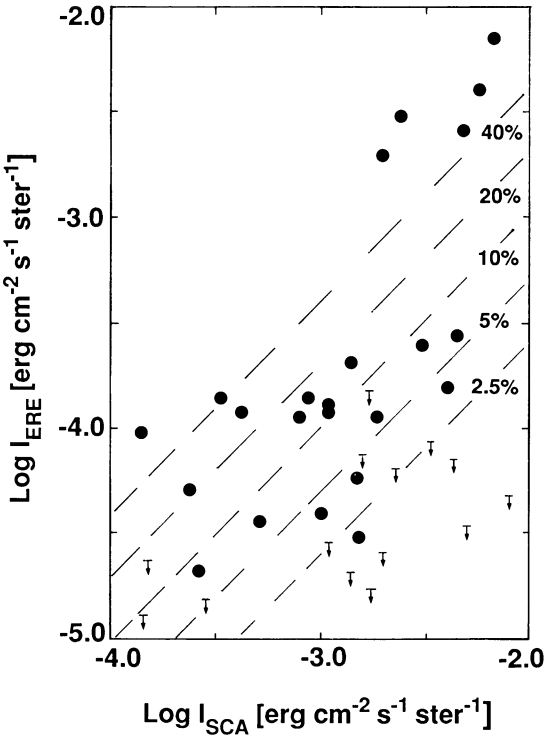

FIG. 1.—The ERE band intensities, uncorrected for interstellar and intranebular extinction, are plotted against nebular scattered light intensities at the same locations. Filled circles represent positive detections; arrows indicate upper limits. The diagonal dashed lines signify different relative intensity levels of ERE to scattered light.

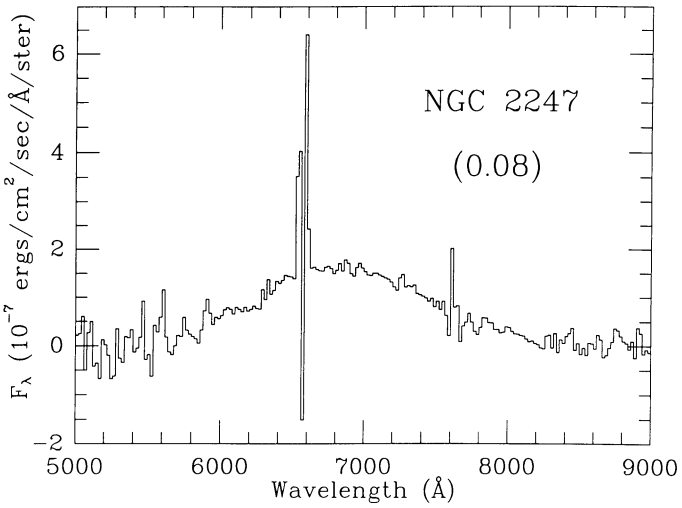

FIG. 2.—The ERE band in NGC 2247 after subtraction of the underlying scattered light spectrum. The features near 6560 Å and 7600 Å are artifacts of the subtraction process and should be disregarded. The ratio of I(ERE)/I(SCA) is 0.08.

Several important conclusions can be drawn.

1. The Red Rectangle, represented by the five points near the upper right corner of the graph, is clearly an object in a class by itself. It is separated in I_{ERE} by at least one order of magnitude from other nebulae with similar values of I_{SCA}. For some reason, the ERE process is substantially more efficient in this object than in any of the others studied. There appear to be no intermediate objects.

2. The ERE band intensity in ordinary reflection nebulae (other than the Red Rectangle) appears to have a well-defined upper limit near $(1.6^{+0.9}_{-0.6}) \times 10^{-4}$ ergs cm^{-2} s^{-1} sr^{-1}, which varies only slightly over a range of underlying scattered light intensities varying by almost two orders of magnitude. None of the intensities plotted in Figure 1 are corrected for interstellar or intranebular extinction but are shown as observed.

3. Within a given object, the variation in the ratio of I_{ERE}/I_{SCA} is driven primarily by changes in the scattered light intensity. The wide range of color differences in $V-I$ and $V-R$ found by Witt and Schild (1986) for a large sample of reflection nebulae therefore do not always imply that the absolute ERE intensity changes greatly.

4. The lower limit of ERE detections and the upper boundary of ERE upper limits merge. The borderline suggests a limit of ERE detectability by our method at a level where the total ERE represents between 2% and 5% of the scattered light intensity. As expected, most nondetection upper limits occurred in nebulae with relatively high scattered light intensities. The apparent absence of ERE in these nebulae must therefore not be interpreted as real, because actual ERE detections have been made at levels corresponding to most of the upper limit values in nebulae with low scattered light intensities.

b) *The ERE Band Profile*

A typical profile of the ERE band in an ordinary reflection nebula is that of NGC 2247, shown in Figure 2. The number in parentheses here and in subsequent figures indicates the ratio of the ERE band intensity to scattered light intensity, both integrated between the limits of λ5500 and λ8500. The large feature appearing at the wavelength of Hα (6563 Å) and the smaller feature at the position of the telluric A band ($\sim$7600 Å) are artifacts of the scattered light subtraction process, and they should be ignored.

The short-wavelength onset of the ERE band in all our spectra is approximately at λ5400. The central wavelength defined by the half-flux criterion (§ II), averaged over all data in Table 2, is $\langle\lambda_c\rangle = 6766 \pm 160$ Å; the average width of the ERE band, defined by the width centered on λ_c containing half the total band flux, is 778 ± 94 Å. There is a weak positive correlation ($r = 0.58$) between band width and central wavelength. This can best be interpreted, if additional band flux is added asymmetrically, favoring the long-wavelength wing of the band. As a result, there can be a real shift of the central wavelength of the band from object to object, and even within an object, as illustrated in two band profiles for the Red Rectangle in Figure 3. Note that the left ordinate corresponds to the profile at 10″ south of the star, the right ordinate to the profile at 6″ south. The central wavelength/bandwidth values for these two profiles are λ6590/760 Å and λ6839/920 Å, respectively. This range of variation in both values is typical for our data set.

Although the spectra in Figure 3 suggest that the ERE bandwidth increases with decreasing offset distance from the star, such an apparent trend is not supported by other data. Band spectra obtained at 7″ north and 14″ north of the star in the Red Rectangle (sequence 28, 29 in Table 2) show this effect only marginally, λ6581/740 Å and λ6522/700 Å. An opposite trend is apparent in the spectra of NGC 2023, displayed in Figure 4.

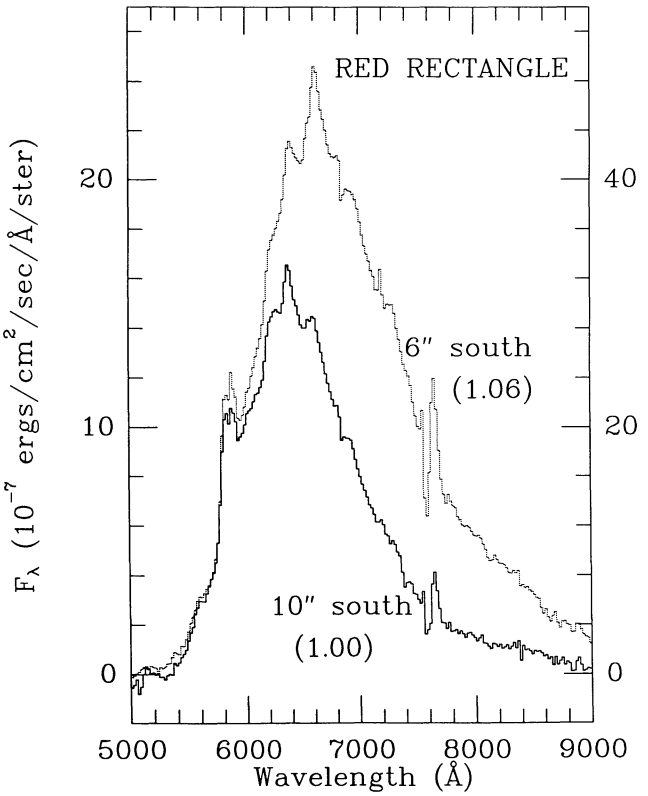

FIG. 3.—The ERE bands in the Red Rectangle 10″ south (*left ordinate*) and 6″ south (*right ordinate*) of HD 44179. The superposed emission features are due to unidentified emissions near 5800, 6380, and 6617 Å, which are unresolved at our resolution.

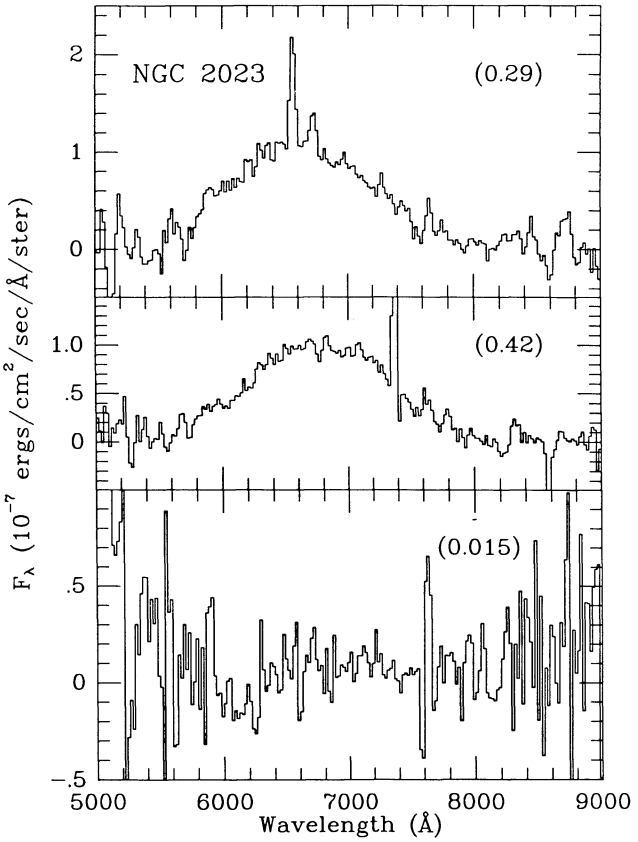

FIG. 4.—ERE band spectra in NGC 2023. The top panel shows the ERE band of a filament located 62″ ENE of HD 37903; the central panel, that of a filament 84″ ENE of HD 37903. The bottom panel shows the wavelength range of the ERE band at 40″ N of HD 37903, for which an upper limit of 0.015 is derived for the ratio I(ERE)/I(SCA).

The top panel presents the ERE band of a filament located 62″ ENE of HD 37903, the central panel that of an adjacent filament at 84″ ENE. The total band intensity is the same in both cases, but the band shifted toward longer wavelengths is now associated with the larger offset, λ6822/800 Å versus λ6673/620 Å. The difference in offset is not necessarily equivalent to actual distances, because we cannot take into account projection effects. A good map of the ERE filaments in NGC 2023 has been published by Witt and Malin (1989). It illustrates that in this object the ERE occurs predominantly in distinct filaments, in addition to more diffuse, fainter regions of ERE, but is absent in other regions. The spectrum of one such ERE-free region is shown in the bottom panel of Figure 4, which corresponds to a spot 40″ N of HD 37903.

Another illustration of the variation of the ERE band strength and the ratio of ERE to scattered light is shown in Figure 5, where four spectra have been extracted from a single exposure on NGC 7023 (sequence 23). The NS slit was placed 20″ W of the star, HD 200775, and the four band profiles correspond to approximate positions (20″W, 0″N), (20″W, 50″N), (20″W, 50″S), and (20″W, 70″S). The first position lies in a featureless region adjacent to HD 200775, the second on the red edge of a globule illuminated by HD 200775, the third on a blue filament, and the fourth on a red filament. The second and fourth regions are distinctly visible as features on the R/B color map of NGC 7023 of WS. It is remarkable that the ERE band intensities at positions 1 and 4 are essentially identical despite a difference in offset distance by a factor 3.6 and a difference in scattered light intensity of nearly a factor 4. The narrowest band (620 Å) of the four centered at the shortest wavelength (6568 Å) corresponds to the intermediate distance of position 3, while the remaining three profiles are essentially indistinguishable.

c) Fine Structure in the ERE Band

The ERE band in the Red Rectangle is known to exhibit sharp emission features superposed on the broad band (Schmidt, Cohen, and Margon 1980; Warren-Smith, Scarrott, and Murdin 1981). These features are most prominent near λλ5800, 6380, and 6617. While our spectral resolution was not optimized for the study of these features, they were nevertheless detected in the spectra of the Red Rectangle. The group of sharp lines near λ5800 is visible as a single feature on the short-wavelength wing of both band spectra shown in Figure 3. Most remarkable is the drastic change in the relative strengths of the λ6380 and the λ6617 features between the two offsets of 6″ and 10″ south. At 10″ south, the λ6617 feature is barely detected, whereas at 6″ south, the same feature dominates the center of the band.

No detection of similar fine structure in the band spectra of other nebulae can be reported from our data. The substantially lower signal strength in those nebulae coupled with the low spectral resolution would make it highly questionable whether similar fine-structure features could have been detected there in the current investigation, if the features are present with similar relative strengths.

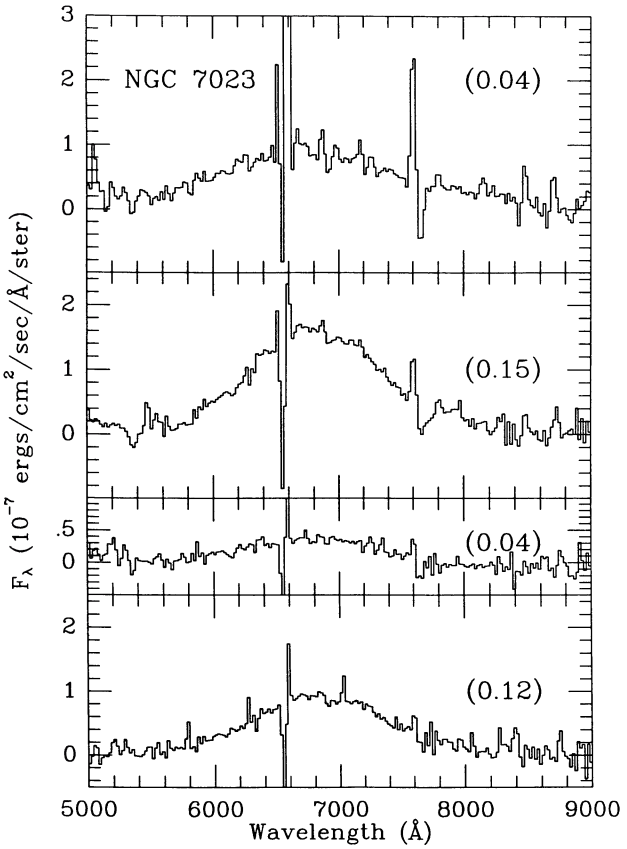

FIG. 5.—ERE band spectra in NGC 7023. The four panels show the variation of band strength and ratio of ERE to scattered light at four positions relative to HD 200775: (20″W, 0″N), (20″W, 50″N); (20″W, 50″S); and (20″W, 70″S).

d) The Scattered Light Spectrum

The detailed comparison of spectra of the illuminating stars and those of the associated reflection nebulae resulted in the determination of the parameter p listed in Tables 2 and 3. A positive value of p indicates a nebular spectrum that is bluer than that of the corresponding illuminating star over the wavelength range of comparison, $\lambda\lambda$5000–9000; a negative value indicates a redder nebular color. The difference in color can be attributed to differences in reddening of stellar and nebular light, to the degree of multiple scattering, to the differences in the wavelength dependence of the dust albedo, to phase function effects, and most often, to the increase in scattering optical depth with decreasing wavelengths. The latter effect renders the nebular color bluer (positive p) than that of the star, unless modified by one of the other effects. Hence, most objects listed in Table 2 and 3 are characterized by positive values of p. Some of the extreme cases of positive p values, NGC 2068 or NGC 1999, are instances where stars are very deeply embedded in the nebulae and substantial multiple scattering occurs. Cases of extremely red nebulae, corresponding to large negative p values, e.g., IC 426, IC 59, and IC 63, occur when nebulae are illuminated under large scattering angles by externally located stars, so that the variation of the phase function asymmetry with wavelength becomes the determining factor. It is important to note that both positive and negative values of p can occur within the same nebula.

There appears to be no correlation between the nebular color and the strength of the ERE band in our data. However, nebular regions scattering under large angles, which tend to be red, also have relatively low surface brightnesses in scattered light. This makes the detection of the ERE band in such objects easier.

IV. DISCUSSION

Three findings of this investigation appear to be particularly significant: (1), the near-constancy of the upper limit of the ERE band intensity in ordinary reflection nebulae independent of apparent offset distance within a nebula and from nebula to nebula; (2), the existence of real variations in the ERE band profile, its width and central wavelength, within a given nebula and from nebula to nebula; and (3), the distinct role of the Red Rectangle in terms of ERE band intensity. We shall discuss these results in sequence.

a) Constancy of the ERE Intensity Upper Limit

The absence of ERE in some nebular regions, while it is clearly present in other regions with similar intensities of dust scattered light, indicates that the presence of dust and abundant stellar photons are necessary but not sufficient conditions for the production of ERE. The near constancy of the maximum ERE intensity level independent of offset distance suggests that the emission originates in a thin spherical shell rather than throughout the nebular volume. To first order, the column density of a thin shell is roughly constant over most of its extent and the density of the exciting stellar radiation at the position of the shell is also constant, resulting in a constant emitted intensity. While the nature of such a shell still requires further study, the spatial association of ERE with radiatively excited fluorescence of molecular hydrogen (Gatley *et al.* 1987; Witt and Schild 1988; Witt *et al.* 1989) strongly suggests that the critical condition for ERE presence is the radiatively driven dissociation of molecular hydrogen occurring in such zones (Stecher and Williams 1967). The results of our study are consistent with the cause of the ERE being the photoluminescence of hydrogenated amorphous carbon. We suggest that amorphous carbon grains which may well be present throughout the entire nebula become hydrogenated only in the warm atomic hydrogen plasma of the H_2 dissociation zone and then become photoluminescent. Laboratory results by Watanabe, Hasegawa, and Kurata (1982) have demonstrated that an increase in the degree of hydrogenation of amorphous carbon by only 20%, from 5.3×10^{22} cm^{-3} to 6.4×10^{22} cm^{-3} hydrogen atoms within the solid, will lead to a doubling of the photoluminescence intensity. Recent results of Landstrass and Ravi (1989) suggest that even fully annealed carbon grains, which are devoid of hydrogen and photoluminescence, can be rehydrogenated completely by immersion into a warm hydrogen plasma.

The physical thickness of the ERE shell in this picture would be determined by the limiting optical depth for stellar radiation in the wavelength range $\lambda\lambda$1108–912, which is responsible for the electronic excitation and associated dissociation of H_2. The opacity to this radiation is quite high due to self-shielding by H_2 as well as to dust extinction (e.g., Federman, Glassgold, and Kwan 1979).

As mentioned previously, our observations of the ERE intensity are uncorrected for any interstellar or intranebular extinction. Where available, the color excesses of the illuminating stars of nebulae with positive ERE detections are of

order $E(B-V) \sim 0.5$, with most of the excess probably due to dust within the nebulae. The extinction of diffuse radiation emitted within the nebula is difficult to estimate, but the effective extinction is likely to be less than the reddening of the star would suggest (e.g., Natta and Panagia 1984). We estimate that the upper limit of ERE intensities for ordinary reflection nebulae shown in Figure 1 after correction for extinction will be near 6×10^{-4} ergs cm^{-2} s^{-1} sr^{-1}.

b) *ERE Band Profile Variations*

The existence of real variations in the ERE band profile and the positive correlation of a bandwidth increase with an increase in the central wavelength are again strong indications for the ERE origin in a solid state luminescence process. As shown in WS, the width and the peak wavelength of the photoluminescence band of hydrogenated amorphous carbon both increase as the degree of hydrogenation is lowered. The decrease of hydrogenation can most easily be achieved by heating the material or by exposure to intense radiation fields. The central wavelengths of the observed ERE bands coincide with the range of wavelength for the band maximum where the luminescence efficiency is near the maximum (Watanabe, Hasegawa, and Kurata 1982). Our spectral resolution was insufficient to shed much light on the problem of the still unidentified narrow emission features superposed on the ERE band of the Red Rectangle, but we note the suggestion by Duley (1988) that attributes these features to narrow luminescence lines observed in terrestrial diamond dust.

The observations showing the band profile variations occurring mainly in the long-wavelength side of the band, together with the positive correlation between bandwidth and central wavelength, are clear arguments against the possibility that these variations are only the apparent results of internal extinction within the nebulae. This process would be expected to produce the opposite results.

c) *The Role of the Red Rectangle*

In the Red Rectangle the ERE band intensity is as much as 25 times larger than it is found in any other reflection nebula; furthermore, the ratio of I_{ERE}/I_{SCA} increases with decreasing angular offset from the star HD 44179. The ERE band strength varies with position in this nebula even more than the scattered light intensity. In these respects the Red Rectangle is an object in a class by itself when compared to the ordinary reflection nebulae. Most of the latter are segments of molecular clouds in which low-mass star formation is occurring (Witt and Schild 1986). The composition of these clouds is likely to be that of average interstellar clouds, with the dust being average as well. The Red Rectangle is a bipolar nebula of rather uncertain evolutionary status (Cohen *et al.* 1975; Dainty *et al.* 1985). The spectrum of HD 44179, a B9–A0 III suspected binary, shows evidence of extreme carbon richness (Sitko 1983). The structure of the nebula suggests an origin through an intense mass-loss process, so that the dust would be locally produced, relatively young material. Recent near-IR speckle observations of the Red Rectangle by Leinert and Haas (1989) have produced evidence showing HD 44179 not to be in the center of the Red Rectangle. It is suggested that the actual source of the mass loss is an object deeply enshrouded at the core of the nebula, with HD 44179 located slightly nearer to the observer, providing the UV and visible luminosity needed for the excitation of the ERE and the observed dust scattered light. The Red Rectangle appears to be a unique object, and the very special geometry suggested by Leinert and Haas may be the explanation.

Our observation of an increase of I_{ERE}/I_{SCA} with decreasing offset distance is also consistent with a geometry where most of the dust is beyond HD 44179 as seen from Earth. ERE will be emitted isotropically whereas dust scattering is strongly forward directed at visible wavelengths; hence, only material predominantly behind HD 44179 will show the observed ratio of I_{ERE}/I_{SCA}. The UV extinction curve of HD 44179 (Sitko, Savage, and Mead 1981) supports the suggestion that the dust in the Red Rectangle is quite unlike that in the general interstellar medium and is probably locally produced from a carbon-rich plasma. The high ERE intensity is a result of the unprocessed nature of the dust, which we assume to have formed as hydrogenated amorphous carbon in situ and to be present in that form throughout the nebula.

V. SUMMARY

1. The extended red emission (ERE) present in many reflection nebulae has been explored spectroscopically. In the $5000 < \lambda < 9000$ Å range, the ERE is due to a broad emission band which appears qualitatively identical to that known previously only in the Red Rectangle nebula. We attribute this band to the photoluminescence of hydrogenated amorphous carbon (HAC) grains.

2. We find the maximum ERE band intensity within individual reflection nebulae and among different nebulae to be remarkably constant, while the associated scattered light intensities vary by close to two orders of magnitude. We interpret this as resulting from shell sources of rehydrogenated amorphous carbon grains found mainly in H_2 dissociation zones.

3. There are true variations in the central wavelengths ($6500 < \lambda_c < 7000$ Å) and the band half-widths ($600 < \Delta\lambda < 1000$ Å) of the ERE bands observed in different locations. A weak positive correlation exists between these two quantities. This is consistent with the HAC model, resulting from different degrees of hydrogenation.

4. The Red Rectangle nebula appears unique in at least three aspects. The ERE intensity in this object is at least one order of magnitude greater than that in any other object observed; sharp emission features are superposed upon the broad ERE band and are found to be variable with offset distance; the ERE band intensity varies with position in a manner analogous to that of the scattered light. We interpret these results as indicating that HAC grains exist throughout the Red Rectangle nebula, having been formed locally through rapid mass loss from a central star. The optically visible star HD 44179 is the source of illumination for this nebula but probably not the cause of the nebula.

We are grateful to the Director of the McGraw-Hill Observatory for the allocation of observing time, and to Matt Johns and the observatory staff for excellent technical support. We thank R. E. Schild and D. G. Furton for the critical reading of an earlier form of this paper and for their constructive criticism. Partial funding for this research was provided by NSF grant AST-8418183 to The University of Toledo.

REFERENCES

Cohen, M., *et al.* 1975, *Ap. J.*, **196**, 179.
Dainty, J. C., Pipher, J. L., Lacasse, M. G., and Ridgway, S. T. 1985, *Ap. J.*, **293**, 530.
Duley, W. W. 1988, *Ap. Space Sci.*, **150**, 387.
Federman, S. R., Glassgold, A. E., and Kwan, J. 1979, *Ap. J.*, **227**, 466.
Gatley, I., *et al.* 1987, *Ap. J.* (*Letters*), **318**, L73.
Landstrass, M. I., and Ravi, K. V. 1989, *Appl. Phys. Letters*, **55**, 975.
Leinert, Ch., and Haas, M. 1989, *Astr. Ap.*, **221**, 110.
Natta, A., and Panagia, N. 1984, *Ap. J.*, **287**, 228.
Schmidt, G. D., Cohen, M., and Margon, B. 1980, *Ap. J.* (*Letters*), **239**, L133.
Sitko, M. L. 1983, *Ap. J.*, **265**, 848.
Sitko, M. L., Savage, B. D., and Meade, M. R. 1981, *Ap. J.*, **246**, 161.
Stecher, T. P., and Williams, D. A. 1967, *Ap. J.* (*Letters*), **149**, L29.
Warren-Smith, R. F., Scarrott, S. M., and Murdin, P. 1981, *Nature*, **292**, 317.
Watanabe, I., Hasegawa, S., and Kurata, Y. 1982, *Japanese J. Appl. Phys.*, **21**, 856.
Witt, A. N., and Malin, D. F. 1989, *Ap. J.* (*Letters*), **347**, L25.
Witt, A. N., and Schild, R. E. 1985, *Ap. J.*, **294**, 225.
———. 1986, *Ap. J. Suppl.*, **62**, 839.
———. 1988, *Ap. J.*, **325**, 837 (WS).
Witt, A. N., Schild, R. E., and Kraiman, J. B. 1984, *Ap. J.*, **281**, 708.
Witt, A. N., Stecher, T. P., Boroson, T. A., and Bohlin, R. C. 1989, *Ap. J.* (*Letters*), **336**, L21.

TODD A. BOROSON: National Optical Astronomy Observatories, P.O. Box 26732, Tucson, AZ 85726-6732

ADOLF N. WITT: Ritter Observatory, The University of Toledo, Toledo, OH 43606